

## An Interface-Capturing Regularization Method for Solving the Equations for Two-Fluid Mixtures

Jian Du<sup>1,\*</sup>, Robert D. Guy<sup>4</sup>, Aaron L. Fogelson<sup>2,3</sup>, Grady B. Wright<sup>5</sup> and James P. Keener<sup>2,3</sup>

<sup>1</sup> Department of Mathematical Science, Florida Institute of Technology, Melbourne, FL 32901, USA.

<sup>2</sup> Department of Mathematics, University of Utah, Salt Lake City, UT 84112, USA.

<sup>3</sup> Department of Bioengineering, University of Utah, Salt Lake City, UT 84112, USA.

<sup>4</sup> Department of Mathematics, University of California Davis, Davis, CA 95616, USA.

<sup>5</sup> Department of Mathematics, Boise State University, Boise, ID 83725, USA.

Received 18 May 2012; Accepted (in revised version) 21 March 2013

Available online 5 July 2013

---

**Abstract.** Many problems in biology involve gels which are mixtures composed of a polymer network permeated by a fluid solvent (water). The two-fluid model is a widely used approach to describe gel mechanics, in which both network and solvent coexist at each point of space and their relative abundance is described by their volume fractions. Each phase is modeled as a continuum with its own velocity and constitutive law. In some biological applications, free boundaries separate regions of gel and regions of pure solvent, resulting in a degenerate network momentum equation where the network volume fraction vanishes. To overcome this difficulty, we develop a regularization method to solve the two-phase gel equations when the volume fraction of one phase goes to zero in part of the computational domain. A small and constant network volume fraction is temporarily added throughout the domain in setting up the discrete linear equations and the same set of equations is solved everywhere. These equations are very poorly conditioned for small values of the regularization parameter, but the multigrid-preconditioned GMRES method we use to solve them is efficient and produces an accurate solution of these equations for the full range of relevant regularization parameter values.

**AMS subject classifications:** 76T99, 76D07, 76D27, 65F22, 76M20, 65M12

**Key words:** Gel swelling, preconditioner, two-fluid model.

---

\*Corresponding author. *Email addresses:* [jdu@fit.edu](mailto:jdu@fit.edu) (J. Du), [guy@math.ucdavis.edu](mailto:guy@math.ucdavis.edu) (R. D. Guy), [fogelson@math.utah.edu](mailto:fogelson@math.utah.edu) (A. L. Fogelson), [wright@math.boisestate.edu](mailto:wright@math.boisestate.edu) (G. B. Wright), [keener@math.utah.edu](mailto:keener@math.utah.edu) (J. P. Keener)

# 1 Introduction

An important class of gels are those composed of a polymer network and fluid solvent. Because of their multiphase and multiscale nature, such gels can exhibit chemical stresses in addition to viscoelastic stresses, which result in swelling and deswelling behavior. These gels are important in many biological systems. For example, the cytoplasm of cells contains a large amount of the protein actin. Actin forms a filamentous gel that can actively contract with the involvement of another protein called myosin [1]. Another important biological gel is mucus which lines the airways of the lung and the surfaces of the stomach and intestines. It can substantially change its volume in response to changes in its ionic environment [2–4]. A gel made of the protein fibrin forms as part of the blood clotting process. When a blood clot forms inside a vein or artery, the fibrin gel grows from the vascular wall into the blood plasma [5–8]. For mucus and fibrin in particular, the gel is adjacent to a fluid in which there is no polymer.

The two-fluid model is a widely used approach to describe gel mechanics [9–16]. In this model, both network and solvent coexist at each point of space, and each phase (network and solvent) is modeled as a continuum with its own velocity field and constitutive law. In this paper, we assume the viscous terms are dominant and inertial terms are negligible. The system of equations describing the two-phase gel dynamics is

$$(\theta^n)_t + \nabla \cdot (\theta^n \mathbf{u}^n) = 0, \tag{1.1}$$

$$(\theta^s)_t + \nabla \cdot (\theta^s \mathbf{u}^s) = 0, \tag{1.2}$$

$$\nabla \cdot (\theta^n \boldsymbol{\sigma}^n) - \zeta \theta^n \theta^s (\mathbf{u}^n - \mathbf{u}^s) - \theta^n \nabla p = \nabla (\theta^n \psi(\theta^n)), \tag{1.3}$$

$$\nabla \cdot (\theta^s \boldsymbol{\sigma}^s) - \zeta \theta^n \theta^s (\mathbf{u}^s - \mathbf{u}^n) - \theta^s \nabla p = 0. \tag{1.4}$$

Here Eqs. (1.1) and (1.2) are continuity equations for the network and solvent, with volume fractions  $\theta^n$ ,  $\theta^s$ , and velocities  $\mathbf{u}^n$  and  $\mathbf{u}^s$ , respectively, and  $0 \leq \theta^n \leq 1$ . Adding these two equations, and using  $\theta^n + \theta^s = 1$  gives the incompressibility constraint

$$\nabla \cdot (\theta^n \mathbf{u}^n + \theta^s \mathbf{u}^s) = 0. \tag{1.5}$$

In the force balance equations (1.3) and (1.4),  $\boldsymbol{\sigma}^n$  and  $\boldsymbol{\sigma}^s$  are stress tensors for the two phases, which are governed by appropriate constitutive laws. For this paper, we assume that both materials are Newtonian fluids, so that the stress tensors are given by

$$\boldsymbol{\sigma}^n = \mu_n (\nabla \mathbf{u}^n + \nabla \mathbf{u}^{nT}) + \lambda_n \delta_{ij} \nabla \cdot \mathbf{u}^n, \tag{1.6}$$

$$\boldsymbol{\sigma}^s = \mu_s (\nabla \mathbf{u}^s + \nabla \mathbf{u}^{sT}) + \lambda_s \delta_{ij} \nabla \cdot \mathbf{u}^s. \tag{1.7}$$

Here  $\mu_{n,s}$  are shear viscosities and  $\lambda_{n,s} + 2\mu_{n,s}/d$  are the bulk viscosities of the network and solvent ( $d$  is the dimension). The network and solvent are also subject to an interphase frictional drag, which is modeled by  $\zeta \theta^n \theta^s (\mathbf{u}^n - \mathbf{u}^s)$ , where  $\zeta > 0$  is the drag coefficient.  $p$  is the single pressure felt by both phases. The term  $\theta^n \psi(\theta^n)$  is an additional pressure which

can be used to represent osmotic effects [17, 18] that can cause the mixture to swell or deswell, or to represent active-contractile processes such as those in the cell cytoplasm [19]. We have developed numerical algorithms for solving these equations in the cases that the solvent phase is a viscous fluid and the network phase is either a viscous fluid [20] or an Oldroyd-B viscoelastic fluid [21].

Many biological problems involve free boundaries whose dynamics are determined as part of the solution. These boundaries may separate regions of gel and regions of pure solvent, e.g. the edge of a growing fibrin clot [22] or at the luminal edge of the mucus layer lining the stomach [3]. The network momentum equation is degenerate in the region with  $\theta^n = 0$  and the network velocity is not well-defined there. Two classes of numerical methods for solving the equations of motion when free boundaries exist between regions occupied by different materials are interface tracking methods and interface capturing methods. In interface tracking methods, the location of the interface is followed explicitly, and different PDEs, which are coupled by matching conditions, are solved on the two sides of the interface [23]. By contrast, interface capturing methods track the interface implicitly. Phase-field methods [24] and level-set methods [25] are interface capturing methods. These methods involve solving the same equations throughout the domain, and they are designed to capture the correct interface conditions.

In this paper, we develop an interface capturing method to solve free-boundary problems which involve a two-phase viscous fluid mixture in contact with a single-phase viscous fluid. To do this, we regularize the equations in regions where the network volume fraction is zero by adding a small and spatially uniform concentration, denoted by  $\epsilon$ , of network so that a well-defined network velocity can be determined by solving the two-fluid equations in the entire domain. The network velocity in the zero-network phase region does not affect the physical network motion because there is no network there to move. We show through numerical tests that the regularization process gives the correct network velocity and volume fraction within the gel. Our method is able to compute an accurate solution efficiently despite the fact that the regularized equations are very poorly conditioned for  $\epsilon$  small. This is possible because the multigrid preconditioning we use with GMRES to solve the equations does an excellent job even in the limit that  $\epsilon \rightarrow 0$ .

The remainder of the paper is organized as follows. In Section 2, we first demonstrate through 1-D analysis, that a well-defined network velocity can be obtained in the limit  $\theta^n \rightarrow 0$ . Based on the analysis, we then propose a numerical method to solve the system of equations for the case  $\theta^n = 0$  in part of the domain. In Section 3, we present 2-D numerical results which illustrate the accuracy of the method by comparing with 1-D analytical and numerical results. We also discuss the possible effects of the parameter choice in our method. We conclude the paper with some remarks in Section 4.

## 2 Regularizations

### 2.1 Analysis: velocity field of the vanishing phase

In this section we derive the leading order equations in 1D to show that in the limit of no network, the velocity is well defined. We assume the solvent viscosity is zero to simplify the analysis since in real biological gels, the network is often more viscous than the fluid solvent by several orders of magnitude. The 1D equations for the velocity are

$$(\alpha_n \theta^n (u^n)_x)_x - \theta^n p_x - (\psi(\theta^n) \theta^n)_x - \zeta \theta^s \theta^n (u^n - u^s) = 0, \tag{2.1}$$

$$-\theta^s p_x - \zeta \theta^s \theta^n (u^s - u^n) = 0, \tag{2.2}$$

$$(\theta^s u^s + \theta^n u^n)_x = 0, \tag{2.3}$$

where  $\alpha_n = 2\mu_n + \lambda_n$ . We impose that the average velocity is zero, and so this last equation becomes

$$\theta^s u^s + \theta^n u^n = 0. \tag{2.4}$$

Using Eq. (2.2) to eliminate the pressure gradient and (2.4) to eliminate the solvent velocity, we get the single equation for the network velocity

$$(\alpha_n \theta^n (u^n)_x)_x - (\theta^n \psi(\theta^n))_x - \frac{\zeta \theta^n}{1 - \theta^n} u^n = 0. \tag{2.5}$$

From this equation we can derive the jump conditions to be satisfied at places where there is a discontinuity in the volume fraction. The jump conditions are

$$[\alpha_n \theta^n (u^n)_x - \theta^n \psi(\theta^n)] = 0, \tag{2.6}$$

$$[u^n] = 0, \tag{2.7}$$

which are continuity of stress and continuity of the network velocity.

Let the domain be the whole real line, and consider a piecewise constant profile of the volume fraction

$$\theta^n = \begin{cases} \theta_-^n, & \text{if } x < 0, \\ \theta_+^n, & \text{if } x > 0. \end{cases} \tag{2.8}$$

For this  $\theta^n$  profile, the solution to (2.5) with the matching conditions (2.6)-(2.7) is

$$u^n = \begin{cases} C \exp(\beta_- x), & \text{if } x < 0, \\ C \exp(-\beta_+ x), & \text{if } x > 0, \end{cases} \tag{2.9}$$

where

$$\beta_{\pm} = \sqrt{\frac{\zeta}{\alpha_n (1 - \theta_{\pm}^n)}}, \tag{2.10}$$

and

$$C = \frac{-\theta_+^n \psi(\theta_+^n) + \theta_-^n \psi(\theta_-^n)}{\alpha_n (\theta_+^n \beta_+ + \theta_-^n \beta_-)}. \tag{2.11}$$

From this solution, we can see that the network velocity is well-behaved in the limit  $\theta_+^n \rightarrow 0$ . Specifically the limiting network velocity for  $x > 0$  is

$$u^n(x) = \psi(\theta_-^n) \left( \frac{1 - \theta_-^n}{\alpha_n \zeta} \right)^{\frac{1}{2}} \exp \left( - \left( \frac{\zeta}{\alpha_n} \right)^{\frac{1}{2}} x \right). \tag{2.12}$$

We show that this is the solution of the limiting form of (2.5) as follows. Since  $\theta^n = \theta_+^n$  is constant for  $x > 0$ , Eq. (2.5) simplifies to

$$\alpha_n (u^n)_{xx} - \frac{\zeta}{1 - \theta_+^n} u^n = 0 \tag{2.13}$$

in this region. In the limit  $\theta_+^n \rightarrow 0$ , this reduces to

$$\alpha_n (u^n)_{xx} - \zeta u^n = 0, \tag{2.14}$$

and  $u^n(x)$  given in (2.12) clearly satisfies this equation.

### 2.2 Numerical method

The analysis from the previous sections suggests an approach for numerically solving the two-fluid equations when regions of space contain only solvent. Given the network volume fraction  $\theta^n$ , we solve for the velocity everywhere in space (including regions with  $\theta^n = 0$ ) after first adding a small constant to the network volume fraction. That is, we make the substitution

$$\theta^n \rightarrow \theta^n + \epsilon \tag{2.15}$$

only when solving for the velocities, where  $\epsilon$  is a small positive number. Thus in regions of space where there is no network, we solve the equations as if there is a small and spatially constant amount of network. Above we showed that the network momentum equation is well-behaved in this limit and gives a velocity that satisfies the correct matching conditions. For brevity, we refer to our regularization method in later sections as the “ $\epsilon$ -method”.

The basic strategy we use for solving the model equations (1.1) and (1.3)-(1.5) is as follows:

1. For a given  $\theta^n$  at time  $t$ , solve the discrete system (1.3)-(1.5) for  $\mathbf{u}^n$ ,  $\mathbf{u}^s$ , and  $p$  at time  $t$ .
2. With velocity field  $\mathbf{u}^n$ , solve for  $\theta^n$  (and thus  $\theta^s$ ) at time  $t + \Delta t$  for (1.1).
3. Repeat step 1, with the  $\theta^n$  at  $t + \Delta t$ .

In two dimension (1.3)-(1.5) can be written in matrix-vector form as

$$\underbrace{\begin{bmatrix} \mathcal{L}_n - \mathcal{C} & \mathcal{C} & -\mathcal{G}_n \\ \mathcal{C} & \mathcal{L}_s - \mathcal{C} & -\mathcal{G}_s \\ -\mathcal{D}_n^T & -\mathcal{D}_s^T & 0 \end{bmatrix}}_{\mathcal{A}^h} \begin{bmatrix} \mathbf{u}^n \\ \mathbf{u}^s \\ p \end{bmatrix} = \begin{bmatrix} \nabla(\theta^n \psi(\theta^n)) \\ 0 \\ 0 \end{bmatrix}, \tag{2.16}$$

where

$$\mathcal{L}_{n,s} = \begin{bmatrix} \alpha_{n,s} \partial_x (\theta^{n,s} \partial_x) + \mu_{n,s} \partial_y (\theta^{n,s} \partial_y) & \mu_{n,s} \partial_y (\theta^{n,s} \partial_x) + \lambda_{n,s} \partial_x (\theta^{n,s} \partial_y) \\ \mu_{n,s} \partial_x (\theta^{n,s} \partial_y) + \lambda_{n,s} \partial_y (\theta^{n,s} \partial_x) & \alpha_{n,s} \partial_y (\theta^{n,s} \partial_y) + \mu_{n,s} \partial_x (\theta^{n,s} \partial_x) \end{bmatrix},$$

$$\mathcal{C} = \begin{bmatrix} \zeta \theta^n \theta^s & 0 \\ 0 & \zeta \theta^n \theta^s \end{bmatrix}, \quad \mathcal{G}_{n,s} = \begin{bmatrix} \theta^{n,s} \partial_x \\ \theta^{n,s} \partial_y \end{bmatrix}, \quad \mathcal{D}_{n,s} = \begin{bmatrix} \partial_x \theta^{n,s} \\ \partial_y \theta^{n,s} \end{bmatrix},$$

and  $\alpha_{n,s} = (2\mu_{n,s} + \lambda_{n,s})$ . All equations in (2.16) are discretized using second-order, centered finite differences, as described in Appendix A. The discretized equations lead to a large, sparse linear system of saddle point type. For a given distribution of the network volume fraction  $\theta^n$ , we use multigrid-preconditioned GMRES to solve the momentum and incompressibility equations together. The detailed algorithm to solve the momentum and incompressibility equations can be found in [20]. The discretized equations lead to a large, sparse linear system of saddle point type. Note that in (2.16), both operators  $\mathcal{L}_{n,s}$  and  $\mathcal{D}_{n,s}$  include volume fractions inside the spatial derivative. When volume fractions are spatially variable, methods for Stokes equations that decouple the velocity and the pressure, such as the pressure-Poisson formulation, cannot be used. The success of such methods relies on the commutation of the Laplacian and divergence operators, which requires constant coefficient operators. Therefore we use a method which solves for both velocities and the pressure simultaneously. For a given distribution of the network volume fraction  $\theta^n$ , we use multigrid-preconditioned GMRES to solve the momentum and incompressibility equations together. The detailed algorithm to solve the momentum and incompressibility equations can be found in [20]. After getting the velocity, the transport equation (1.1) is solved by the second-order high-resolution Godunov scheme as described in Appendix B.

### 3 Numerical results and comparisons

We have two kinds of test problems, differing in whether the coefficient  $\zeta$  for drag between the two fluids is set to zero. For the first problem, we set  $\zeta = 0$  so that we can derive an analytic solution (see Appendix) with which to compare the numerical results. For the second problem with nonzero drag, we instead compare our numerical results with the numerical solutions from a one dimensional moving mesh, free boundary code. For all test problems, the computational domain is the square  $[-1,1] \times [-1,1]$ , and an initial network volume fraction distribution

$$\theta^n = \begin{cases} \frac{1}{6}, & \text{if } 0 \leq \sqrt{x^2 + y^2} \leq \frac{1}{3}, \\ 0, & \text{if } \sqrt{x^2 + y^2} > \frac{1}{3} \end{cases}$$

is used. Homogeneous Dirichlet boundary conditions are used for  $\mathbf{u}^n$  and  $\mathbf{u}^s$  on the sides of the square domain. For these tests we assume that the gel has a preferred volume fraction of  $\theta^n = 0.1$  and we prescribe a linear swelling pressure function

$$\psi(\theta^n) = (\theta^n - 0.1), \tag{3.1}$$

so that the gel tends to swell if  $\theta^n < 0.1$  and to de-swell if  $\theta^n > 0.1$ . For these parameters, the equilibrium radius of the gel is about 0.43.

### 3.1 Zero drag

For this set of numerical tests, the drag coefficient between the two fluids is set to zero. The viscosities for the network are set as  $\mu_n = 0.1$  and  $\lambda_n = 0$ , so that the time scale of swelling is 1 (from (C.22)). Because the solvent viscosity is often much less than that of the network in real gels, we set  $\mu_s = 10^{-6}\mu_n$ . A value  $\epsilon = 10^{-9}$  is used to solve the momentum equations. The plots of  $\theta^n$  and  $\mathbf{u}^n$  at time  $t = 0$  and 1 from a  $256 \times 256$  grid computation are shown in Fig. 1.

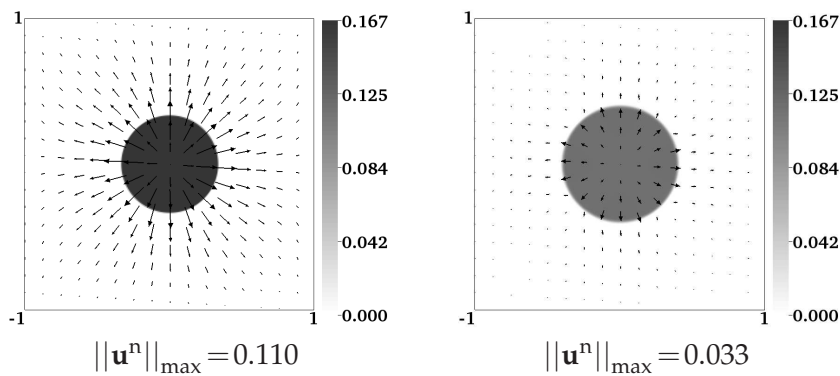


Figure 1:  $\theta^n$  distribution along with the vector fields of  $\mathbf{u}^n$  at  $t=0$  (left) and  $t=1$  (right).  $256 \times 256$  grid.

In Fig. 2 we plot the distribution of  $\theta^n$  and the radial component of the network velocity  $u_r^n$  along the positive  $y$ -axis from our numerical simulations ( $128 \times 128$  grid). The 1D radially-symmetric analytical solution based on (C.16), (C.19) and (C.22) (with  $\mu_s = 0$ ) are shown with solid black lines. The plots indicate that the method does an excellent job of capturing the dynamics of the network. The interface remains sharp as time evolves and the numerical network velocity matches well with the analytical solution in the region where there is network. For these numerical simulations, homogeneous Dirichlet boundary conditions for the network velocity were imposed on the boundary of the computational domain. For the 1D-radially symmetric problem, the motion of the gel is not affected by the single-fluid outside of the gel, and so the question arises of whether the numerical boundary conditions on the domain boundary have a significant affect on the numerical solution within the gel. Later in the paper (Section 3.3), we show that the solution is insensitive to the numerical boundary conditions.

In Fig. 3 we display the relative errors in the volume fraction and in the velocity at time  $t = 0.25$  and  $t = 2$  as the mesh is refined. For the volume fraction, we show the one-norm of the error both for the region with nonzero  $\theta^n$  (i.e. in the gel) as well as over the whole domain. As in Fig. 3(a,c), we see that the rate of convergence for the

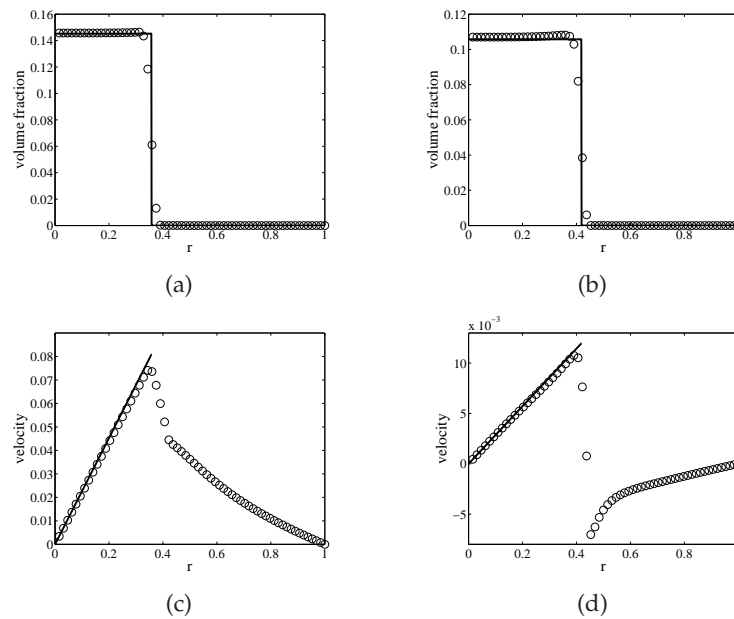


Figure 2:  $\theta^n$  profiles at times  $t=0.25$  (a) and  $t=2.0$  (b), and radial velocity  $u_r^n$  along the positive  $y$ -axis at times  $t=0.25$  (c) and  $t=2.0$  (d). Analytical solutions are shown in solid lines.

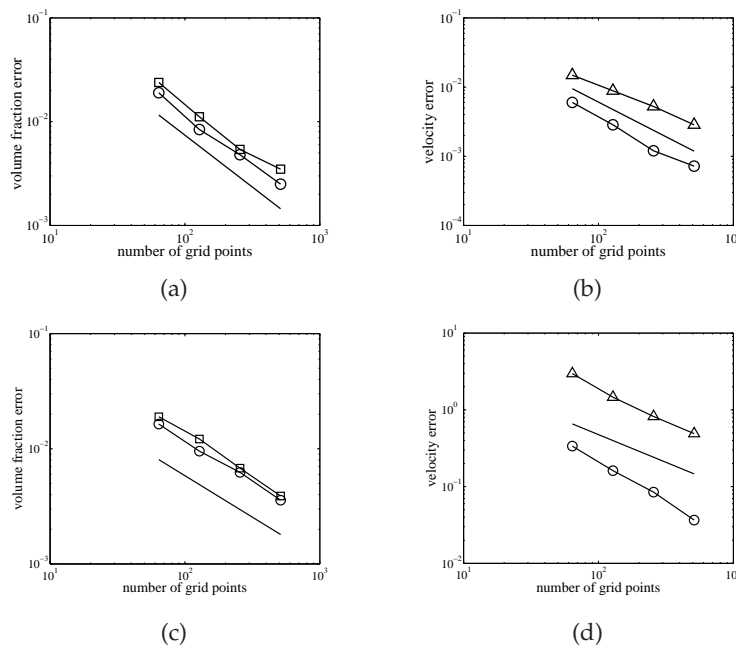


Figure 3: Relative errors in  $\theta^n$  (left) and  $u^n$  (right). Solid straight lines show first-order convergence. One-norm errors of volume fraction computed in gel only (circles) and entire domain (squares) at  $t=0.25$  (a) and  $t=2.0$  (c). One-norm errors (circles) and max-norm errors (triangles) of velocity computed in gel only at  $t=0.25$  (b) and  $t=2.0$  (d).

volume fraction is about first-order in the one-norm, both within the gel and the whole domain. In Fig. 3(b,d) the errors of the velocity within the gel show better than first-order convergence in the one-norm and first-order convergence in the max-norm. Though the velocity plots in Fig. 2(c) and (d) of the no-network region exhibit large deviation from the analytical results, we do observe about first-order convergence for the network velocity (not shown) over the whole domain. The results illustrate that the network velocity in the no-network region is well-behaved as  $h \rightarrow 0$ .

## 3.2 Nonzero drag

In this section, we present tests in which the drag coefficient  $\zeta$  is not zero. We begin by determining values of  $\zeta$  which are ‘small’, ‘medium’, and ‘large’. Then we compare results obtained by the  $\epsilon$ -method with results obtained by solving the one-dimensional radially-symmetric equations numerically using a moving mesh method in which the interface location is explicitly tracked.

### 3.2.1 Determining the test parameters

In polar coordinates, consider a situation in which the network volume fraction is uniformly equal to  $\theta_0^n$  for  $0 \leq r \leq R(0)$ . The corresponding network velocity and pressure are then functions of  $\beta r$  where

$$\beta = \sqrt{\frac{\zeta}{\mu_n(1-\theta_0^n)}}. \quad (3.2)$$

The parameter  $\beta$  defines an inverse length scale. The smaller this length scale (and thus the larger  $\beta$ ) is compared to the length scale of the domain of the problem (which is 1 for our tests), the greater the drag force is compared to the network viscous force. As in the tests for the zero drag case, we let  $\theta_0^n = 1/6$ ,  $\psi = \theta^n - 0.1$ , and  $R(0) = 1/3$ . We run simulations with three values of  $\beta$ : 1, 10, 100, which correspond to low, medium, and high drag. For this set up, the initial velocity and pressure are (using  $R = R(0)$ ) given by

$$p = \frac{(I_0(\beta r) - I_0(\beta R))}{\beta R I_0(\beta R) - I_1(\beta R)} \theta_0^n \psi(\theta_0^n) \beta R, \quad (3.3)$$

$$u^n(r) = \frac{\psi(\theta_0^n) R}{2\mu_n(\beta R I_0(\beta R) - I_1(\beta R))} I_1(\beta r), \quad (3.4)$$

where  $I_n$  is the modified Bessel function of order  $n$ . See Appendix C.1 for the derivation. For each  $\beta$ , we set  $\mu_n$  to

$$\mu_n = \frac{\psi(\theta_0^n) R I_1(\beta R)}{2(\beta R I_0(\beta R) - I_1(\beta R))} \quad (3.5)$$

and

$$\zeta = 2\mu_n \beta^2 (1 - \theta_0^n). \quad (3.6)$$

With this choice, the initial radial velocity is 1 at the initial gel boundary  $r = R(0)$ . The three sets of  $(\beta, \mu_n, \zeta)$  are given in Table 1. For these computations,  $\mu_s$  is set to  $10^{-8}$ .

Table 1: Values of  $\mu_n$  and  $\zeta$  used in the numerical tests with the linear swelling pressure and radially-symmetric initial volume fraction as determined by (3.5) and (3.6).

$\beta$	$\mu_n$	$\zeta$
1	$1.08 \cdot 10^{-2}$	$1.80 \cdot 10^{-2}$
10	$3.70 \cdot 10^{-3}$	$6.16 \cdot 10^{-1}$
100	$3.38 \cdot 10^{-4}$	5.64

### 3.2.2 Comparison of $\epsilon$ -method and 1-D moving mesh method

In this section we describe refinement studies of the  $\epsilon$ -method (with drag coefficient  $\zeta \neq 0$ ) by comparing with solutions generated by the moving mesh method described in the Appendix. For the moving mesh simulations, we used 2000 mesh points and set the time steps according to the CFL condition with Courant number 0.75. We experimented with more points, and the comparisons were essentially unchanged. We used the same initial conditions and numerical parameters as in Section 3.1 and computed the solution for the three sets of  $(\mu_n, \zeta)$  values shown in Table 1. All simulations were run until time  $t = 0.1$ . At this time, for all three parameter value sets, the network was still far from equilibrium, i.e., it was still swelling.

Fig. 4 shows the  $\theta^n$  and  $u_r^n$  distributions along the positive  $y$ -axis at time  $t = 0.1$ . A  $128 \times 128$  grid is used for the  $\epsilon$ -method simulations. The results indicate that the  $\epsilon$ -method captures the correct behavior for the system. In Fig. 5 we plot  $\theta^n$  profiles from simulations with different grid sizes and compare them with solutions from the moving mesh method. It is clear that there is less smearing of the interface as the grid is refined and that the smearing does not grow noticeably in time.

In Fig. 6, we present the results from a refinement study. To compute the errors, we linearly interpolate the fine-grid, moving-mesh solution to the fixed Cartesian grid. We compare the  $x$ -component of  $\mathbf{u}^n$  computed by the two methods. Thus we are only computing the errors where the network is nonzero in the moving-mesh method. We see that approximately first-order convergence is obtained in both the one-norm and max-norm.

### 3.3 Effects of boundary conditions and $\epsilon$

In this section, we study the performance of the  $\epsilon$ -method with different choices of parameter  $\epsilon$  and different boundary conditions. To verify our earlier statement that the boundary conditions for the no gel region do not affect the solutions inside the gel, we redo the test from Section 3.1, changing the boundary condition in the  $x$ -direction from Dirichlet to periodic (for both  $\theta^n$ ,  $\mathbf{u}^n$  and  $\mathbf{u}^s$ ), while keeping all the other parameters unchanged. Fig. 7 shows the  $\theta^n$  and  $u_r^n$  profiles along the positive  $x$ -axis for the two types of boundary conditions. We see that the solutions within the gel are visually indistinguishable at this scale.

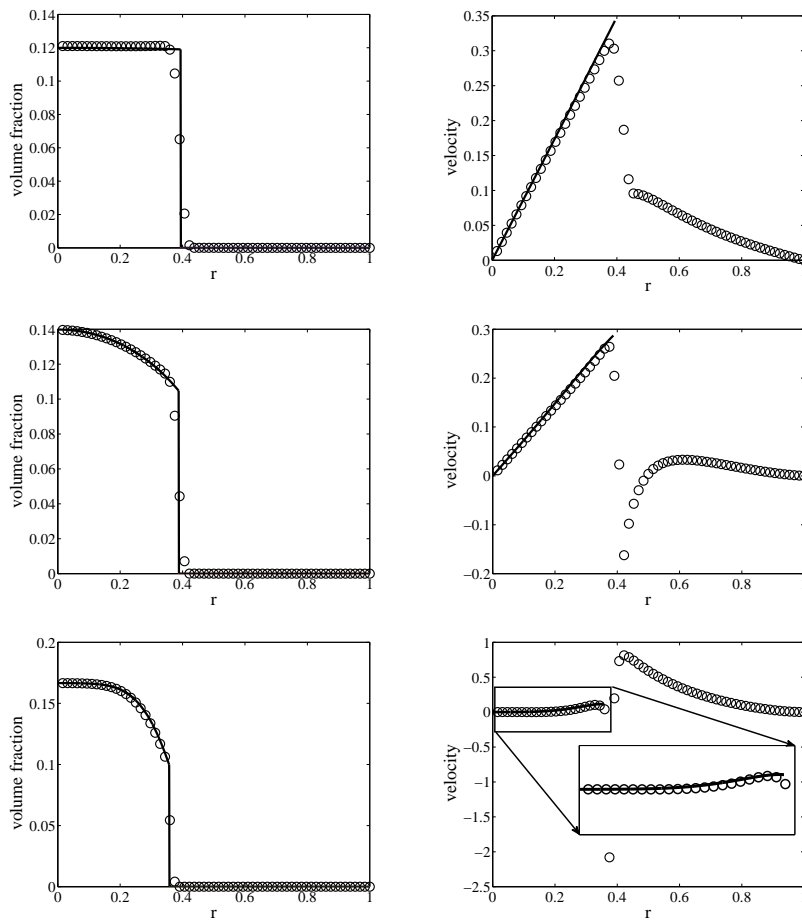


Figure 4: Comparison of  $\theta^n$  (left) and  $u_r^n$  (right) at  $t=0.1$  for a radially-symmetric test problem with drag. Top  $\beta=1$ , middle  $\beta=10$ , bottom  $\beta=100$ . Heavy solid lines are results from moving mesh calculation. Circles show  $\epsilon$ -method results with a  $128 \times 128$  grid. Inset in lower-right panel shows closeup of the network velocity inside the gel.

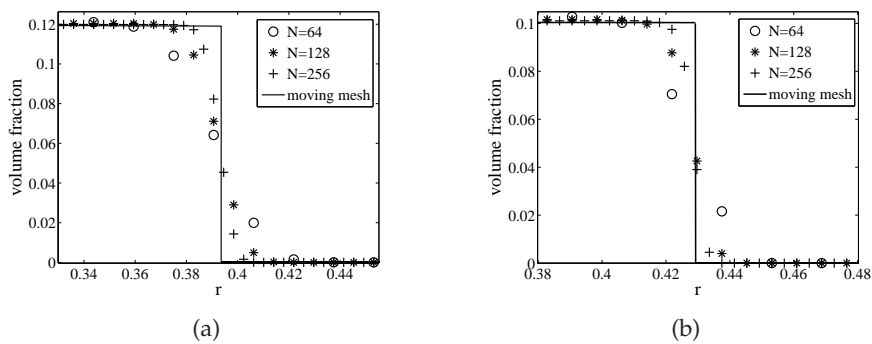


Figure 5:  $\theta^n$  profiles at  $t=0.1$  (a) and  $t=0.5$  (b) for different grid sizes.  $\beta = 1$ .

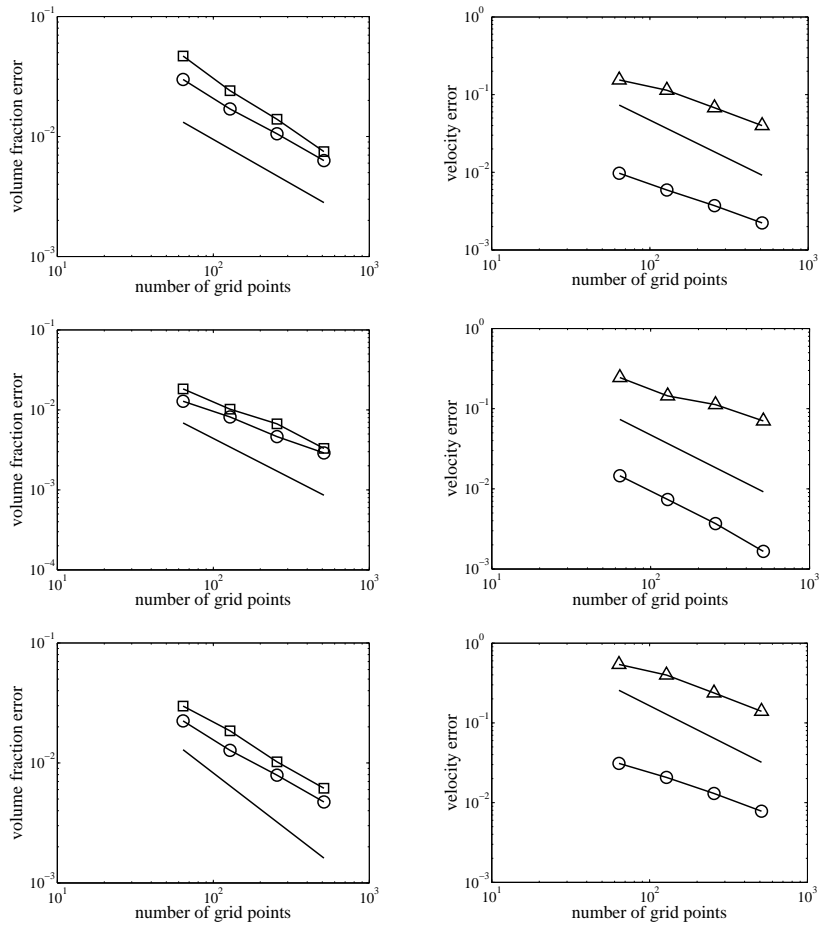


Figure 6: Relative errors in  $\theta^n$  (left) and  $u^n$  (right) at  $t=0.1$  for  $\beta=1$  (top), 10 (middle), 100 (bottom). One norm (circles) and max-norm (squares) of errors computed in gel only. Solid lines indicate first-order convergence.

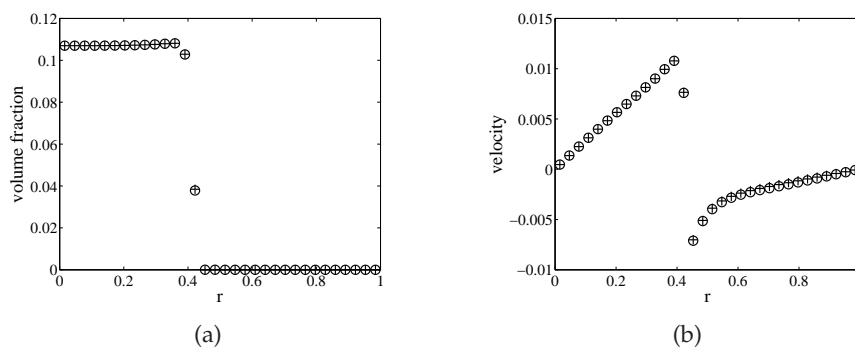


Figure 7:  $\theta^n$  (a) and  $u_r^n$  (b) at  $t=2.0$  with Dirichlet (circles) or periodic (cross) domain boundary conditions.

As seen from the numerical results in Section 3.1 and 3.2, the  $\epsilon$ -method works very well in dealing with problems involving zero network volume fractions. The results in those sections were obtained with  $\epsilon = 10^{-9}$ . It is an important question whether the accuracy of our algorithm is sensitive to the choice of  $\epsilon$ . For the original discrete system (2.16), we expect severe conditioning problems as  $\epsilon$  approaches zero. Indeed the PDE system itself is not well-posed in this limit. In practice, we solve a preconditioned version of the linear system, and so the question becomes whether our preconditioning approach is effective even in the limit that  $\epsilon$  goes to zero. If it is not, then the computational costs of the iteration might become unacceptably large for small values of  $\epsilon$  and the accuracy of the resulting solution would be questionable.

To explore these issues, we revisit the test problem of Section 3.1. We use a fixed  $\theta^n$  distribution and keep all parameters other than  $\epsilon$  constant. We perform a series of calculation on a  $64 \times 64$  grid for values of  $\epsilon$  ranging from  $10^{-22}$  to  $10^{-2}$ . The results are shown in Table 2. For the entire range of  $\epsilon$  values examined, the iteration count is no higher than 7. The table also shows that the error in the network  $x$ -velocity (where  $\theta^n \neq 0$ ), calculated by comparing the  $x$ -component of the computed and the analytical network velocity, drops somewhat with  $\epsilon$  over the range  $10^{-2}$  to  $10^{-7}$  but is insensitive to further reduction in  $\epsilon$ . The performance of the method for different grid sizes with fixed  $\epsilon = 10^{-12}$  is shown in Table 3. As the grid is refined, the number of iterations for the solver to converge remain within a reasonable range. The errors of the  $x$ -velocity for the network indicate that a better than first-order convergence is obtained. Thus, from both an accuracy and a computational work perspective, there is great freedom in the choice of the parameter  $\epsilon$ .

Table 2: Performance of the linear system solver for (2.16) for different  $\epsilon$  values, grid size  $64 \times 64$ . Number of iterations is required by the preconditioned GMRES solver to reduce the relative residual below a tolerance of  $10^{-6}$ .

$\epsilon$	# of iterations	$\  \text{error } u^n \ _1$
$10^{-2}$	4	$1.99 \times 10^{-3}$
$10^{-7}$	6	$5.93 \times 10^{-4}$
$10^{-12}$	7	$6.46 \times 10^{-4}$
$10^{-17}$	7	$6.46 \times 10^{-4}$
$10^{-22}$	7	$6.46 \times 10^{-4}$

Table 3: Performance of the linear system solver for (2.16) for different grid sizes,  $\epsilon = 10^{-12}$ . The number of iterations is that required by the preconditioned GMRES solver to reduce the relative residual below a tolerance of  $10^{-6}$ .

	$64 \times 64$	$128 \times 128$	$256 \times 256$	$512 \times 512$
# of iterations	7	10	12	12
$\  \text{error } u^n \ _1$	$6.46 \times 10^{-4}$	$2.35 \times 10^{-4}$	$8.65 \times 10^{-5}$	$3.73 \times 10^{-5}$

To get a better understanding of the convergence of the multigrid-preconditioned solver, we investigate the spectra of the original and preconditioned operators for the

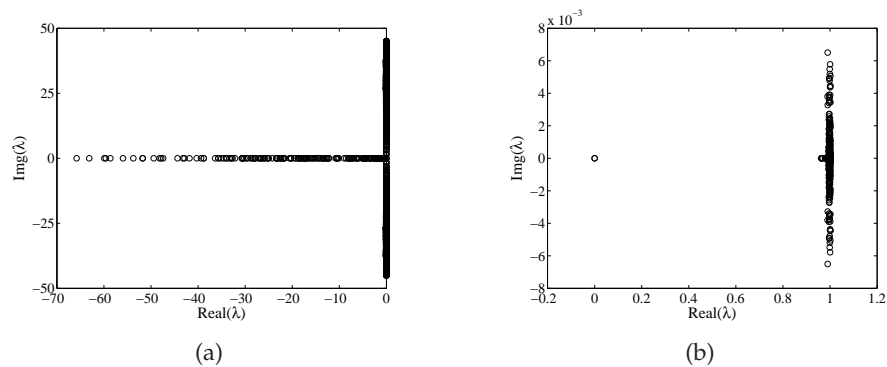


Figure 8: Eigenvalues of  $\mathcal{A}^h$  (a) and  $\mathcal{A}^h(\mathcal{M}^h)^{-1}$  (b). Note the different scales on the plots in (a) and (b). The grid size is  $32 \times 32$  and  $\epsilon = 10^{-12}$ .

system. If we let  $y^T = [(\mathbf{u}^n)^T (\mathbf{u}^s)^T p^T]$  and  $f$  be the right hand side of (2.16), the preconditioned system of equations to solve with GMRES is given by

$$\mathcal{A}^h(\mathcal{M}^h)^{-1}z = f, \tag{3.7}$$

where  $z = \mathcal{M}^h y$ , and  $\mathcal{M}^h$  represents the preconditioning matrix from the multigrid scheme. We can build the preconditioning operator column-by-column by applying the multigrid scheme, with zero initial guess, to right hand sides consisting of successive columns of the identity matrix (see [20] for details). With a grid size of  $32 \times 32$  and  $\epsilon = 10^{-12}$ , the eigenvalues of  $\mathcal{A}^h$  and  $\mathcal{A}^h(\mathcal{M}^h)^{-1}$  are shown in Fig. 8. See Fig. 9 (bottom row) for plots of the magnitudes of these eigenvalues. Without any preconditioner, the eigenvalues of  $\mathcal{A}^h$  are not clustered in the complex plane and their magnitudes are fairly evenly distributed between  $10^{-12}$  ( $\approx \epsilon$ ) and  $10^2$ . On the other hand, the spectrum for the preconditioned matrix  $\sigma(\mathcal{A}^h(\mathcal{M}^h)^{-1})$  is clustered very close to  $\lambda = 1$ . A detailed examination of the plot reveals that three of the eigenvalues for the preconditioned matrix are close to 0, and one is numerically zero. This latter eigenvalue corresponds an eigenvector consisting of zero velocity components and constant pressure. It is easy to show that the spectrum of the multigrid iteration matrix is simply  $1 - \sigma(\mathcal{A}^h(\mathcal{M}^h)^{-1})$ . Therefore, the corresponding eigenvalues of the multigrid iteration matrix are clustered very close to zero, with only a few outliers. This helps to explain the convergence behavior of the preconditioned GMRES solver (see [28, 29] for more details).

In Fig. 9, we plot the magnitude of the eigenvalues for  $\mathcal{A}^h$  and  $\mathcal{A}^h(\mathcal{M}^h)^{-1}$ , ordered from smallest to largest for three different values of  $\epsilon$ . It is clear from the plot that unlike their unpreconditioned counterparts, the magnitude of the eigenvalues for the preconditioned matrix only exhibit very small variations with different  $\epsilon$ . This explains the good performance of the preconditioned solver for the wide range of the regularization parameter.

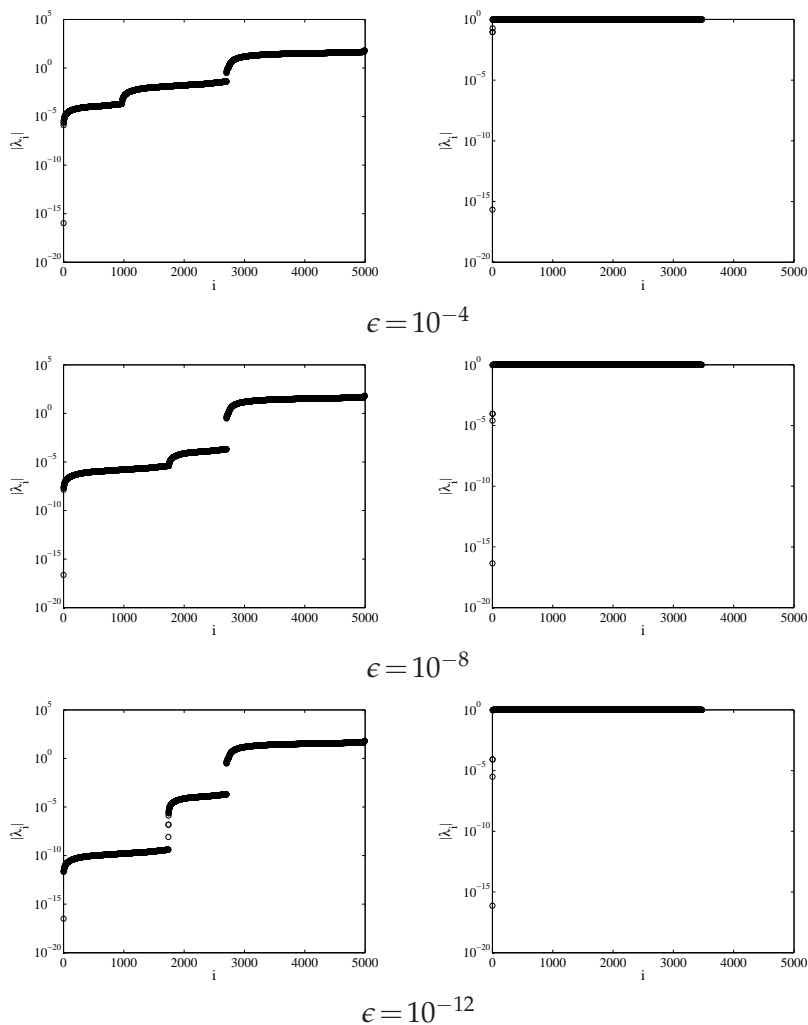


Figure 9: Magnitude of eigenvalues for  $\mathcal{A}^h$  (left) and  $\mathcal{A}^h(\mathcal{M}^h)^{-1}$  (right) for different values of  $\epsilon$ . Grid size is  $32 \times 32$ .

## 4 Conclusion

Many fluids in biology (gels) are mixtures of polymer network and fluid solvent. An appealing approach to describing them is the two-fluid mixture model, in which each component of the mixture is a continuum with its own volume fraction, velocity and constitutive law. For many applications, the volume fraction of the network phase is zero in part of the domain, and, in those regions, the system of PDEs is not well-defined. As the result, the strategy of solving a single set of equations everywhere is problematic. We previously developed numerical methods for situations in which volume fractions for both fluids are nonzero. However, the resulting linear system becomes extremely ill-

conditioned when one of the volume fractions goes to zero and special treatment of the problem is needed.

In this paper we explore a simple interface-capturing method that consists of a regularization procedure to solve the two-fluid model equations describing gels composed of two viscous fluids, in the situation in which the volume fraction of one fluid vanishes in part of the domain. A small and constant network volume fraction is temporarily added throughout the domain in setting up the discrete linear equations. The multigrid-preconditioned Krylov algorithm we introduced in [20] is then used to solve this regularized system.

We have presented several numerical experiments for a swelling gel in contact with a single phase fluid. When there is no frictional force between the two fluids, the numerical results show excellent agreement with the analytical solutions. For problems with frictional force, simulation results from the regularization method match well with those from a moving mesh method in which the gel interface is explicitly computed. For all the test problems, the method exhibits about first-order convergence. While the regularized equations themselves become increasingly ill-conditioned as the regularization parameter  $\epsilon$  approaches zero, our results also indicate that, with our preconditioner, the accuracy and computational cost of the method are not sensitive to the choice of  $\epsilon$ .

### Acknowledgments

This work was supported, in part, by NSF Grant DMS-0540779, DMS-1160432 and NIH Grant RO1-GM090203. R.D.G. was additionally supported by UCOP Grant 09-LR-03-116724-GUYR. G.B.W. was additionally supported by NSF Grant DMS-0934581 and DMS-1160379.

### A Spatial discretization of the momentum equations

We use second order centered finite differences on the staggered grid displayed in Fig. 10 to discretize the spatial derivatives in the momentum equations and volume-averaged incompressibility constraint. This leads to the following approximation of the first row of (2.16) at the interior point  $(x_{i+\frac{1}{2},j}, y_{i+\frac{1}{2},j})$ :

$$\begin{aligned}
 & \frac{\alpha_n}{h^2} \left[ \theta_{i+1,j}^n (u_{i+\frac{3}{2},j}^n - u_{i+\frac{1}{2},j}^n) - \theta_{i,j}^n (u_{i+\frac{1}{2},j}^n - u_{i-\frac{1}{2},j}^n) \right] \\
 & + \frac{\mu_n}{h^2} \left[ \bar{\theta}_{i+\frac{1}{2},j+\frac{1}{2}}^n (u_{i+\frac{1}{2},j+1}^n - u_{i+\frac{1}{2},j}^n) - \bar{\theta}_{i+\frac{1}{2},j-\frac{1}{2}}^n (u_{i+\frac{1}{2},j}^n - u_{i+\frac{1}{2},j-1}^n) \right] \\
 & + \frac{\mu_n}{h^2} \left[ \bar{\theta}_{i+\frac{1}{2},j+\frac{1}{2}}^n (v_{i+1,j+\frac{1}{2}}^n - v_{i,j+\frac{1}{2}}^n) - \bar{\theta}_{i+\frac{1}{2},j-\frac{1}{2}}^n (v_{i+1,j-\frac{1}{2}}^n - v_{i,j-\frac{1}{2}}^n) \right] \\
 & + \frac{\lambda_n}{h^2} \left[ \theta_{i+1,j}^n (v_{i+1,j+\frac{1}{2}}^n - v_{i+1,j-\frac{1}{2}}^n) - \theta_{i,j}^n (v_{i,j+\frac{1}{2}}^n - v_{i,j-\frac{1}{2}}^n) \right] \\
 & - \bar{\zeta} \bar{\theta}_{i+\frac{1}{2},j}^n \bar{\theta}_{i+\frac{1}{2},j}^s (u_{i+\frac{1}{2},j}^n - u_{i+\frac{1}{2},j}^s) - \bar{\theta}_{i+\frac{1}{2},j}^n \frac{p_{i+1,j} - p_{i,j}}{h} = \frac{\psi(\theta_{i+1,j}^n) - \psi(\theta_{i,j}^n)}{h}, \tag{A.1}
 \end{aligned}$$

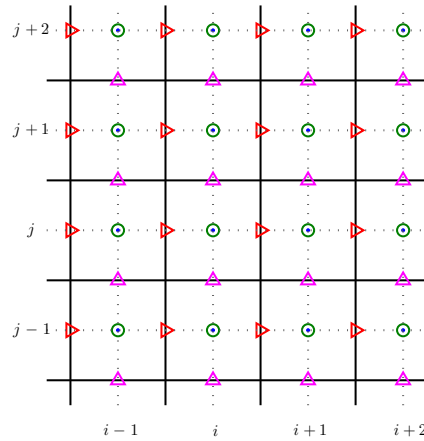


Figure 10: Location of the unknowns in the MAC grid for the 2-D gel model: ▷=network/solvent  $x$ -velocity, △=network/solvent  $y$ -velocity, ●=pressure, and ○=network/solvent volume fractions.

$h$  is the mesh spacing. The approximation to the second row at the interior point  $(x_{i,j+\frac{1}{2}}, y_{i,j+\frac{1}{2}})$  is given by:

$$\begin{aligned} & \frac{\mu_n}{h^2} \left[ \bar{\theta}_{i+\frac{1}{2},j+\frac{1}{2}}^n (u_{i+\frac{1}{2},j+1}^n - u_{i+\frac{1}{2},j}^n) - \bar{\theta}_{i-\frac{1}{2},j+\frac{1}{2}}^n (u_{i-\frac{1}{2},j+1}^n - u_{i-\frac{1}{2},j}^n) \right] \\ & + \frac{\lambda_n}{h^2} \left[ \theta_{i,j+1}^n (u_{i+\frac{1}{2},j+1}^n - u_{i-\frac{1}{2},j+1}^n) - \theta_{i,j}^n (u_{i+\frac{1}{2},j}^n - u_{i-\frac{1}{2},j}^n) \right] \\ & + \frac{\alpha_n}{h^2} \left[ \theta_{i,j+1}^n (v_{i,j+\frac{3}{2}}^n - v_{i,j+\frac{1}{2}}^n) - \theta_{i,j}^n (v_{i,j+\frac{1}{2}}^n - v_{i,j-\frac{1}{2}}^n) \right] \\ & + \frac{\mu_n}{h^2} \left[ \bar{\theta}_{i+\frac{1}{2},j+\frac{1}{2}}^n (v_{i+1,j+\frac{1}{2}}^n - v_{i,j+\frac{1}{2}}^n) - \bar{\theta}_{i-\frac{1}{2},j+\frac{1}{2}}^n (v_{i,j+\frac{1}{2}}^n - v_{i-1,j+\frac{1}{2}}^n) \right] \\ & - \zeta \bar{\theta}_{i,j+\frac{1}{2}}^n \bar{\theta}_{i,j+\frac{1}{2}}^s (v_{i,j+\frac{1}{2}}^n - v_{i,j+\frac{1}{2}}^s) - \bar{\theta}_{i,j+\frac{1}{2}}^n \frac{p_{i,j+1} - p_{i,j}}{h} = \frac{\psi(\theta_{i,j+1}^n) - \psi(\theta_{i,j}^n)}{h}. \end{aligned} \tag{A.2}$$

Bars over  $\theta^n$  and  $\theta^s$  represent arithmetic averages of the values of these variables at nearest neighbor cells with two-point averages when there is a mix of integer and half-integer indices, and four-point averages when there are two half-integer indices. The discretizations of the third and fourth row of (2.16) are the same, but with variables for the network replaced accordingly by the variables for the solvent. Finally, the last row of (2.16) is approximated at  $(x_{i,j}, y_{i,j})$  by

$$\begin{aligned} & \frac{-\bar{\theta}_{i+\frac{1}{2},j}^n u_{i+\frac{1}{2},j}^n + \bar{\theta}_{i-\frac{1}{2},j}^n u_{i-\frac{1}{2},j}^n}{h} + \frac{-\bar{\theta}_{i,j+\frac{1}{2}}^n v_{i,j+\frac{1}{2}}^n + \bar{\theta}_{i,j-\frac{1}{2}}^n v_{i,j-\frac{1}{2}}^n}{h} \\ & + \frac{-\bar{\theta}_{i+\frac{1}{2},j}^s u_{i+\frac{1}{2},j}^s + \bar{\theta}_{i-\frac{1}{2},j}^s u_{i-\frac{1}{2},j}^s}{h} + \frac{-\bar{\theta}_{i,j+\frac{1}{2}}^s v_{i,j+\frac{1}{2}}^s + \bar{\theta}_{i,j-\frac{1}{2}}^s v_{i,j-\frac{1}{2}}^s}{h} = 0. \end{aligned} \tag{A.3}$$

Where necessary, we use second-order extrapolation to account for the no-slip boundary conditions for velocity field. As in Fig. 10, suppose  $x = x_{i-\frac{3}{2}}$  is the physical domain

boundary. Thus  $v_{i-2,j+\frac{1}{2}}^n$  is located on the ghost cell outside the domain and  $v_{i-\frac{3}{2},j+\frac{1}{2}}^n = 0$  according to the no-slip boundary conditions. By fitting a quadric polynomial at locations  $(i,j+\frac{1}{2}), (i-1,j+\frac{1}{2})$  and  $(i-\frac{3}{2},j+\frac{1}{2})$  with the corresponding y-velocity values, it is easy to get  $v_{i-2,j+\frac{1}{2}}^n = \frac{1}{3}v_{i,j+\frac{1}{2}}^n - 2v_{i-1,j+\frac{1}{2}}^n$  by extrapolation.

## B Solution of the advection equation for $\theta^n$

To advance (1.1) in time we use a variant of the corner transport upwind (CTU) method of Colella [26], which is a conservative, second order, high-resolution, unsplit Godunov method. For notational simplicity, we drop the subscript n from (1.1) in the description of the discretization below, and use  $\theta$  to denote the network volume fraction.

The CTU scheme for advancing (1.1) in time from  $t$  to  $t + \Delta t_k$  at the  $(i,j)$  cell center can be written in conservative form as

$$\theta_{i,j}^{k+1} = \theta_{i,j}^k - \frac{\Delta t_k}{h} \left( F_{i+1/2,j}^{k+1/2} - F_{i-1/2,j}^{k+1/2} + F_{i,j+1/2}^{k+1/2} - F_{i,j-1/2}^{k+1/2} \right), \tag{B.1}$$

where

$$F_{i\pm 1/2,j}^{k+1/2} = \theta_{i\pm 1/2,j}^{k+1/2} u_{i\pm 1/2,j}^{k+1/2}, \tag{B.2}$$

$$F_{i,j\pm 1/2}^{k+1/2} = \theta_{i,j\pm 1/2}^{k+1/2} v_{i,j\pm 1/2}^{k+1/2}. \tag{B.3}$$

The two velocity components at the  $k+1/2$  time level are obtained from linear extrapolations from values at time level  $k$  and  $k-1$ . The values of  $\theta$  at the  $k+1/2$  time level and at the EW and NS edges of the cell centered at  $(i,j)$  are obtained by Taylor series expansions in which temporal derivatives are expressed in terms of spatial derivatives using (1.1). For each cell edge, this results in two approximations to  $\theta$ , one from each of the two cells which share that edge. The approximations at the E and W edges for the  $(i,j)$  cell are given by

$$\begin{aligned} (\theta_{i\pm 1/2,j}^{k+1/2})^{E,W} &= \theta_{i,j}^k + \frac{\Delta t_k}{2} \partial_t \theta_{i,j}^k \pm \frac{h}{2} \partial_x \theta_{i,j}^k \\ &= \theta_{i,j}^k + \left[ \pm \frac{h}{2} - \frac{\Delta t_k}{2} \bar{u}_{i,j}^k \right] \partial_x \theta_{i,j}^k - \frac{\Delta t_k}{2} \theta_{i,j}^k \partial_x u_{i,j}^k - \frac{\Delta t_k}{2} \partial_y \left( v_{i,j}^k \theta_{i,j}^k \right), \end{aligned} \tag{B.4}$$

where E and W correspond to the plus and minus case, respectively. The expression after the second equal sign is obtained by replacing  $\partial_t \theta_{i,j}$  with  $-\nabla \cdot (\mathbf{u}\theta)$  according to the advection equation (1.1), and then applying the product rule to  $\partial_x (u\theta)$ . Similarly, the approximations at the N and south S horizontal edges are given by

$$\begin{aligned} (\theta_{i,j\pm 1/2}^{k+1/2})^{N,S} &= \theta_{i,j}^k + \frac{\Delta t_k}{2} \partial_t \theta_{i,j}^k \pm \frac{h}{2} \partial_y \theta_{i,j}^k \\ &= \theta_{i,j}^k + \left[ \pm \frac{h}{2} - \frac{\Delta t_k}{2} \bar{v}_{i,j}^k \right] \partial_y \theta_{i,j}^k - \frac{\Delta t_k}{2} \theta_{i,j}^k \partial_y v_{i,j}^k - \frac{\Delta t_k}{2} \partial_x \left( u_{i,j}^k \theta_{i,j}^k \right). \end{aligned} \tag{B.5}$$

The cell centered velocities  $\bar{u}_{i,j}^k$  and  $\bar{v}_{i,j}^k$  in (B.4) and (B.5) are obtained by arithmetic averaging of the corresponding edge centered values.

There are two variants of the CTU algorithm that can be followed at this point. Starting with (B.4), the first variant is to approximate  $\partial_x \theta_{i,j}^k$  with limited differencing, approximate  $\partial_x u_{i,j}^k$  with (staggered) centered differencing, and approximate the transverse (conservative) derivative  $\partial_y (v_{i,j}^k \theta_{i,j}^k)$  with upwind differencing. A similar approximation is used for the terms in (B.5). This variant can lead to overshoots or excessive smearing in the solution when it features large gradients that propagate obliquely to the grid [26, p. 182]. The second variant ameliorates this problem and is the one we use in this study. It is identical to the first variant except in the way the transverse derivatives in (B.4) and (B.5) are handled. The method can be viewed as a predictor-corrector method. In the predictor step, (B.4) and (B.5) are approximated without the transverse derivatives terms. The corrector step updates the predicted approximations with the transverse derivatives, where, for example, the volume fractions used in the approximation of  $\partial_y (v_{i,j}^k \theta_{i,j}^k)$  in (B.4) are obtained from the first approximation of (B.5). The update to (B.5) with its transverse derivative is similarly obtained using the predicted approximation from (B.4).

The exact details of the predictor step are as follows. First, the two values of the volume fraction at each cell edge are approximated as

$$(\hat{\theta}_{i\pm 1/2,j}^{k+1/2})^{E,W} = \theta_{i,j}^k + \left[ \pm \frac{h}{2} - \frac{\Delta t_k}{2} \bar{u}_{i,j}^k \right] \partial_x^{mc} \theta_{i,j}^k - \frac{\Delta t_k}{2} \theta_{i,j}^k \partial_x^h u_{i,j}^k, \tag{B.6}$$

$$(\hat{\theta}_{i,j\pm 1/2}^{k+1/2})^{N,S} = \theta_{i,j}^k + \left[ \pm \frac{h}{2} - \frac{\Delta t_k}{2} \bar{v}_{i,j}^k \right] \partial_y^{mc} \theta_{i,j}^k - \frac{\Delta t_k}{2} \theta_{i,j}^k \partial_y^h v_{i,j}^k. \tag{B.7}$$

Dropping the superscript  $k$ , the approximate derivatives operators  $\partial_x^h$  and  $\partial_y^h$  in (B.6) and (B.7) are given by

$$\partial_x^h u_{i,j} = \frac{u_{i+1/2,j} - u_{i-1/2,j}}{h}, \quad \partial_y^h v_{i,j} = \frac{v_{i,j+1/2} - v_{i,j-1/2}}{h}, \tag{B.8}$$

while  $\partial_x^{mc}$  and  $\partial_y^{mc}$  are monotonized central (MC) difference operators [27] and are given by

$$\partial_x^{mc} \theta_{i,j} = \min\text{mod} \left( \frac{\theta_{i+1,j} - \theta_{i-1,j}}{2h}, \min\text{mod} \left( 2 \frac{\theta_{i+1,j} - \theta_{i,j}}{h}, 2 \frac{\theta_{i,j} - \theta_{i-1,j}}{h} \right) \right), \tag{B.9}$$

$$\partial_y^{mc} \theta_{i,j} = \min\text{mod} \left( \frac{\theta_{i,j+1} - \theta_{i,j-1}}{2h}, \min\text{mod} \left( 2 \frac{\theta_{i,j+1} - \theta_{i,j}}{h}, 2 \frac{\theta_{i,j} - \theta_{i,j-1}}{h} \right) \right), \tag{B.10}$$

where

$$\min\text{mod}(a,b) = \begin{cases} a, & \text{if } |a| < |b| \text{ and } ab > 0, \\ b, & \text{if } |b| < |a| \text{ and } ab > 0, \\ 0, & \text{otherwise.} \end{cases}$$

Next, the appropriate approximate edge values  $\hat{\theta}_{i\pm 1/2,j}^{k+1/2}$  and  $\hat{\theta}_{i,j\pm 1/2}^{k+1/2}$  are determined by upwinding:

$$\hat{\theta}_{i\pm 1/2,j}^{k+1/2} = \begin{cases} (\hat{\theta}_{i\pm 1/2,j}^{k+1/2})^E, & \text{if } u_{i\pm 1/2,j}^{k+1/2} \geq 0, \\ (\hat{\theta}_{i\pm 1/2,j}^{k+1/2})^W, & \text{if } u_{i\pm 1/2,j}^{k+1/2} < 0, \end{cases}$$

$$\hat{\theta}_{i,j\pm 1/2}^{k+1/2} = \begin{cases} (\hat{\theta}_{i,j\pm 1/2}^{k+1/2})^N, & \text{if } v_{i,j\pm 1/2}^{k+1/2} \geq 0, \\ (\hat{\theta}_{i,j\pm 1/2}^{k+1/2})^S, & \text{if } v_{i,j\pm 1/2}^{k+1/2} < 0. \end{cases}$$

The corrector step updates the edge values (B.6) and (B.7) as

$$(\theta_{i\pm 1/2,j}^{k+1/2})^{E,W} = (\hat{\theta}_{i\pm 1/2,j}^{k+1/2})^{E,W} - \frac{\Delta t_k}{2} \left( v_{i,j\pm 1/2}^{k+1/2} \hat{\theta}_{i,j\pm 1/2}^{k+1/2} - v_{i,j-1/2}^{k+1/2} \hat{\theta}_{i,j-1/2}^{k+1/2} \right), \tag{B.11}$$

$$(\theta_{i,j\pm 1/2}^{k+1/2})^{N,S} = (\hat{\theta}_{i,j\pm 1/2}^{k+1/2})^{N,S} - \frac{\Delta t_k}{2} \left( u_{i\pm 1/2,j}^{k+1/2} \hat{\theta}_{i\pm 1/2,j}^{k+1/2} - u_{i-1/2,j}^{k+1/2} \hat{\theta}_{i-1/2,j}^{k+1/2} \right). \tag{B.12}$$

The final step of the CTU scheme is to again use upwinding to choose the appropriate approximate edge values  $\theta_{i\pm 1/2,j}^{k+1/2}$  and  $\theta_{i,j\pm 1/2}^{k+1/2}$  for the fluxes in (B.2) and (B.3).

## C Moving gel problems in cylindrical coordinates

We present the equations describing gel dynamics in cylindrical coordinates. Then, for a radially-symmetric situation, we introduce a change of variables to map the gel to a fixed domain and we determine the appropriate conservation equation in the transformed coordinates. For the case of zero drag and initially uniform network volume fraction, we show that the velocity is linear and that the volume fraction remains uniform. An explicit solution is determined for a linear swelling pressure function. Finally, we present the numerical method used to solve the transformed equations in the case of nonzero drag.

### C.1 Gel equations in cylindrical coordinates

We examine the model equations in cylindrical coordinates  $(r, \phi, z)$ . The viscous stress tensor for the network is

$$\sigma^n = 2\mu_n \mathbf{D}^n + \lambda_n (\nabla \cdot \mathbf{u}^n) \delta, \tag{C.1}$$

where  $\mathbf{u}^n = (u_r^n, u_\phi^n, u_z^n)$  is the network velocity, and  $\mathbf{D}^n$  and  $\delta$  are the network deformation rate and unit tensors, respectively. We are interested in problems with radial symmetry, and so we focus on the radial component of the network viscous force density  $\mathbf{e}_r \cdot \nabla \cdot \sigma^n$ .

Under the assumption of radial symmetry, the radial component of the network viscous force density is

$$\mathbf{e}_r \cdot \nabla \cdot \sigma^n = \frac{2}{r} \frac{\partial}{\partial r} \left( \mu_n \theta^n r \frac{\partial u_r^n}{\partial r} \right) - \frac{2\mu_n \theta^n}{r^2} u_r^n + \frac{\partial}{\partial r} \left( \frac{\lambda_n \theta^n}{r} \frac{\partial}{\partial r} (r u_r^n) \right) \tag{C.2}$$

and the radial component of the network viscous stress on a surface whose normal is in the radial direction is

$$\sigma_{rr} = 2\mu_n \frac{\partial u_r^n}{\partial r} + \frac{\lambda_n}{r} \frac{\partial}{\partial r} (ru_r^n). \quad (\text{C.3})$$

We use (C.2) in the network momentum equation and write the model equations for a radially-symmetric problem with an inviscid solvent as

$$\begin{aligned} \frac{2}{r} \frac{\partial}{\partial r} \left( \mu_n \theta^n r \frac{\partial u_r^n}{\partial r} \right) - \frac{2\mu_n \theta^n}{r^2} u_r^n + \frac{\partial}{\partial r} \left( \frac{\lambda_n \theta^n}{r} \left( \frac{\partial}{\partial r} (ru_r^n) \right) \right) \\ = \theta^n \frac{\partial p}{\partial r} + \frac{\partial}{\partial r} (\psi(\theta^n) \theta^n) + \zeta \theta^s \theta^n (u_r^n - u_r^s), \end{aligned} \quad (\text{C.4})$$

$$0 = -\theta^s \frac{\partial p}{\partial r} - \zeta \theta^s \theta^n (u_r^s - u_r^n), \quad (\text{C.5})$$

$$0 = \frac{\frac{\partial}{\partial r} (r\theta^s u_r^s + r\theta^n u_r^n)}{r}. \quad (\text{C.6})$$

Both the solvent velocity and the pressure can be eliminated by integrating the incompressibility constraint (C.6) and then using (C.5). Doing so, we obtain

$$\frac{2}{r} \frac{\partial}{\partial r} \left( \mu_n \theta^n r \frac{\partial u_r^n}{\partial r} \right) - \frac{2\mu_n \theta^n}{r^2} u_r^n + \frac{\partial}{\partial r} \left( \frac{\lambda_n \theta^n}{r} \frac{\partial}{\partial r} (ru_r^n) \right) - \frac{\partial}{\partial r} (\theta^n \psi(\theta^n)) - \frac{\zeta \theta^n}{1 - \theta^n} u_r^n = 0. \quad (\text{C.7})$$

At the edge of the gel, the boundary condition is that there is no stress (assuming the external pressure is zero):

$$\left( 2\mu_n \theta^n \frac{\partial u_r^n}{\partial r} + \frac{\lambda_n \theta^n}{r} \frac{\partial}{\partial r} (ru_r^n) - \theta^n \psi(\theta^n) \right) \Big|_{r=R} = 0, \quad (\text{C.8})$$

where  $r=R$  denotes the boundary of the gel. For spatially uniform  $\theta^n$ , we can solve for  $u_r^n$  from the above two equations. The pressure is recovered from (C.5) and (C.6) assuming that the pressure at the free boundary is zero. The expressions for the solution are given by (3.3) and (3.4).

The conservation equation for the network volume fraction is

$$(\theta^n)_t + \frac{1}{r} \frac{\partial}{\partial r} (ru_r^n \theta^n) = 0. \quad (\text{C.9})$$

## C.2 Moving domain transformation

We assume that the network is nonzero only for  $0 \leq r \leq R(t)$ , and that the network boundary moves according to

$$\frac{dR}{dt} = u_r^n(R^-, t). \quad (\text{C.10})$$

We make a change of coordinates  $r = R(t)\rho$  to map the problem to the fixed domain  $0 \leq \rho \leq 1$ . In terms of the new coordinates, the conservation equation (C.9) becomes

$$(\theta^n)_t - \frac{R'\rho}{R} \frac{\partial \theta^n}{\partial \rho} + \frac{1}{R^2 \rho} \frac{\partial}{\partial \rho} (R \theta^n u_r^n \rho) = 0, \tag{C.11}$$

which is not in conservative form. However, the total amount of gel remains constant, so

$$\int_0^R \theta^n(r, t) r dr = \int_0^1 \theta^n(\rho, t) R^2 \rho d\rho \tag{C.12}$$

is constant. Hence in the new coordinates, it is the quantity  $\theta^n R^2$  that is conserved, and our conservation law should involve the time derivative of  $\theta^n R^2$ . After some manipulation of (C.11), we find that

$$(\theta^n R^2)_t + \frac{1}{\rho} \frac{\partial}{\partial \rho} (R \rho (u_r^n - R' \rho) \theta^n) = 0, \tag{C.13}$$

which is the conservation law in the new coordinate system.

### C.3 Analytic solution for zero drag

We suppose that the drag coefficient  $\zeta = 0$ , and that the network is spatially uniform at time  $t = 0$ . Then the last two terms in (C.7) vanish and the equation implies that the viscous force density is zero throughout the gel. In this situation, the equation for the network velocity (after using  $r = R(t)\rho$ ) is

$$\frac{2}{\rho} \frac{\partial}{\partial \rho} \left( \mu_n \theta^n \rho \frac{\partial u_r^n}{\partial \rho} \right) - \frac{2\mu_n \theta^n}{\rho^2} u_r^n + \frac{\partial}{\partial \rho} \left( \frac{\lambda_n \theta^n}{\rho} \frac{\partial}{\partial \rho} (\rho u_r^n) \right) = 0. \tag{C.14}$$

This equation is solved by the linear function  $u_r^n(\rho, t) = C\rho$  for any constant  $C$ . By definition, the speed of the gel boundary  $R'(t) = u_r^n(1)$ , so  $u_r^n(\rho, t) = R'\rho$ . Upon substituting this into the conservation law (C.13), we find that at  $t = 0$

$$(\theta^n R^2)_t = 0, \tag{C.15}$$

which suggests that the initially uniform  $\theta^n$  will remain uniform. As long as  $\theta^n$  is spatially uniform, the instantaneous velocity is linear in  $\rho$ . So the momentum and conservation equations have a solution of the form

$$\theta^n(t) = \frac{R_0^2 \theta_0^n}{(R(t))^2} = \frac{N_T}{R(t)^2} \tag{C.16}$$

and

$$u_r^n(\rho, t) = R'(t)\rho, \tag{C.17}$$

where  $N_T = \theta_0^n R_0^2$  is the total amount of network. It remains to determine  $R(t)$ . Using the no-stress boundary condition (C.8), the map  $r = R(t)\rho$ , and the relation  $u_r^n(1, t) = R'(t)$ , we find that

$$\frac{dR}{dt} = \frac{\psi(\theta^n(t))}{2(\mu_n + \lambda_n)} R(t), \tag{C.18}$$

from which it follows that

$$u_r^n = \frac{\psi(\theta^n(t))}{2(\mu_n + \lambda_n)} R(t)\rho, \tag{C.19}$$

and

$$\theta^n(t) = \frac{N_T}{(R(t))^2}. \tag{C.20}$$

Substituting (C.20) into (C.18) gives an equation for the motion of the interface

$$\frac{dR^2}{dt} = \frac{\psi(N_T/R^2)}{(\mu_n + \lambda_n)} R^2. \tag{C.21}$$

We give analytic solutions to this equation for the linear swelling pressure function  $\psi = \psi_0(\theta^n - a)$

$$R^2(t) = R_{eq}^2 + (R_0^2 - R_{eq}^2) \exp\left(-\frac{\psi_0 a}{(\mu_n + \lambda_n)t}\right), \tag{C.22}$$

where  $R_{eq}^2 = N_T/a$ . Eqs. (C.16) and (C.19) give the corresponding volume fraction and velocity distributions for the network.

### C.4 Moving mesh, free-boundary code

We suppose that the network volume fraction is only nonzero for  $0 \leq r \leq R(t)$  where  $R(t)$  satisfies (C.10) (i.e. it moves with the network velocity). We introduce the change of spatial variable  $r = R(t)\rho$ , and we define the transformed velocity and volume fraction by

$$v(\rho, t) = u_r^n(r, t), \tag{C.23}$$

$$\Theta(\rho, t) = \theta^n(r, t). \tag{C.24}$$

These functions are defined on the fixed spatial domain  $0 \leq \rho \leq 1$ . Using the expressions derived in Section C.2, these new variables satisfy the system of equations

$$\frac{2}{\rho} \frac{\partial}{\partial \rho} \left( \mu_n \Theta \rho \frac{\partial v}{\partial \rho} \right) - \frac{2\mu_n \Theta}{\rho^2} v + \frac{\partial}{\partial \rho} \left( \frac{\lambda_n \Theta}{\rho} \frac{\partial}{\partial \rho} (\rho v) \right) - R \frac{\partial}{\partial \rho} (\Theta \psi(\Theta)) - R^2 \frac{\xi \Theta}{1 - \Theta} v = 0, \tag{C.25}$$

$$\left( 2\mu_n \Theta \frac{\partial v}{\partial \rho} + \frac{\lambda_n \Theta}{\rho} \frac{\partial (\rho v)}{\partial \rho} - R \Theta \psi(\Theta) \right) \Big|_{\rho=1} = 0, \tag{C.26}$$

$$\frac{\partial}{\partial t} (\Theta R^2) + \frac{1}{\rho} \frac{\partial}{\partial \rho} (R \rho (v - R' \rho) \Theta) = 0, \tag{C.27}$$

$$\frac{dR}{dt} = v(1, t). \tag{C.28}$$

We use a finite volume discretization in which the domain is divided into  $N$  volumes. The spatially average volume fractions are approximated by their values at the volume centers  $\rho_j^c = (j-1)\Delta\rho$  for  $j=1, \dots, N$ , and the velocities are approximated at the volume edges  $\rho_j^e = (j-1/2)\Delta\rho$  for  $j=1, \dots, N$ . We use Strang splitting for advancing the system in time, alternating between solving for the velocity and updating the volume fraction and gel length. We use second-order accurate solvers for each of the sub-steps. For advancing the volume fraction we use a conservative, Lax-Wendroff-like update. In the transformed problem, there are no sharp interfaces, and the solution stays smooth. Therefore there is no need to use limiters.

## References

- [1] B. Alberts, A. Johnson, J. Lewis, M. Raff, K. Roberts, and P. Walter, *Molecular Biology of the Cell*, Garland Science, New York, 2007.
- [2] J.V. Fahy and B. R. Dickey, *Airway Mucus Function and Dysfunction*, *N. Engl. J. Med.*, 363(2010), 2233-47.
- [3] Sören Schreiber and Peter Scheid, *Gastric mucus of the guinea pig: Proton carrier and diffusion barrier*, *Am. J. Physiol. Gastrointest, Liver Physiol.*, 272(1997), G63-G70.
- [4] P. Verdugo, I. Deyrup-Olsen, A.W. Martin and D. L. Luchtel, *Polymer gel phase transition: The molecular mechanism of product release in mucin secretion*, *Mechanics of Swelling*, Springer-Verlag, NATO ASI Series (1992), H64 671-681.
- [5] J.W. Weisel, *Fibrinogen and Fibrin*, *Adv. Protein Chem.*, 70 (2005), 247-299.
- [6] K.C. Gersh, K.E. Edmondson and J. W. Weisel, *Flow rate and fibrin fiber alignment*, *J. Thromb. Haemost.*, 8(2010), 2826-8.
- [7] R.A. Campbell, M.M. Aleman, L.D. Gray, M.R. Falvo and A.S. Wolberg, *Flow Profoundly Influences Fibrin Network Structure: Implications for Fibrin Formation and Clot Stability in Hemostasis*, *Thromb. Haemost.*, 104(2010), 1281-4.
- [8] K.B.Neeves, D.A. Illing and S.L. Diamond, *Thrombin flux and wall shear rate regulate fibrin fiber deposition state during polymerization under flow*, *Biophys. J.*, 98(2010), 1344-52.
- [9] V. H. Barocas and R. T. Tranquillo, *An anisotropic biphasic theory of tissue-equivalent mechanics: The interplay among cell traction, fibrillar network deformation, fiber alignment, and cell contact guidance*, *J. Biomech. Eng.*, 119 (1997), 137-145.
- [10] H. Byrne and L. Preziosi, *Modelling solid tumour growth using the theory of mixtures*, *Math. Med. Biol.*, 20 (2003), 341-366.
- [11] N.G. Cogan and R.D. Guy, *Multiphase flow models of biogels from crawling cells to bacterial biofilms*, *HFSP J.*, 4(2010), 11-25.
- [12] X. He and M. Dembo, *On the mechanics of the first cleavage division of the sea urchin egg*, *Exp. Cell. Res.*, 233 (1997), 252-273.
- [13] J. P. Keener and S. Sircar and A. L. Fogelson, *Kinetics of swelling gels*, *SIAM J. Appl. Math.*, 71 (2011), 854-875.
- [14] A. J. Levine and F. C. MacKintosh, *The mechanics and fluctuation spectrum of active gels*, *J. Phys. Chem. B*, 113 (2009), 3820-3830.
- [15] V. C. Mow and M. H. Holmes and W. M. Lai, *Fluid transport and mechanical properties of articular cartilage: A review*, *J. Biomech.*, 17 (1984), 377-394.
- [16] C. W. Wolgemuth and A. Mogilner and G. Oster, *The hydration dynamics of polyelectrolyte gels with applications to cell motility and drug delivery*, *Eur. Biophys. J.*, 33 (2004), 146-158.

- [17] M. Doi and H. See, *Introductin to Polymer Physics*, Oxford University Press, Oxford, England, 1996.
- [18] T. Tanaka and D. J. Fillmore, Kinetics of swelling in gels, *J. Chem. Phys.*, 70 (1979), 1214-1218.
- [19] W. Alt and M. Dembo, Cytoplasm dynamics and cell motion: two-phase flow models. *Math. Biosci.*, 156 (1999), 207-28.
- [20] G.B. Wright, R.D. Guy and A.L. Fogelson, An efficient and robust method for simulating two-phase gel dynamics, *SIAM J. Sci. Comput.*, 30(2008), 2535-2565.
- [21] G.B. Wright, R.D. Guy, J. Du and A.L. Fogelson, A high-resolution finite-difference method for simulating two-fluid, viscoelastic gel dynamics, *J. Non-Newton. Fluid Mech.*, 166(2011), 1137-1157.
- [22] R.D. Guy, A.L. Fogelson and J. P. Keener, Modeling Fibrin Gel Formation in a Shear Flow, *Mathematical Medicine and Biology*, 24(2007), 111-130.
- [23] J. Glimm, J.W. Grove, X. Li, K.-M. Shyue, Y. Zeng and Q. Zhang, Three dimensional front tracking, *SIAM J. Sci. Comp.*, 19(1998), 703-727.
- [24] W. J. Boettinger, J. A. Warren, C. Beckermann and A. Karma, Phase-field simulation of solidification, *Annu. Rev. Mater. Res.*, 32 (2002), 163-94.
- [25] S. Osher and J. Sethian, Front propagating with curvature dependent speed: algorithms based on Hamilton-Jacobi formulations, *J. Comput. Phys.*, 79(1988), 12-49.
- [26] P. Colella, Multidimensional upwind methods for hyperbolic conservation laws, *J. Comput. Phys.*, 87(1990), 171-200.
- [27] B. van Leer, Towards the ultimate conservative difference scheme, V. A second order sequel to Godunov's method, *J. Comput. Phys.*, 32(1979), 101-136.
- [28] T. Washio and C. W. Oosterlee, Krylov subspace acceleration for nonlinear multigrid schemes, *Electron. Trans. Numer. Anal.*, 6 (1997), 271-290.
- [29] C. W. Oosterlee and T. Washio, An evaluation of parallel multigrid as a solver and a preconditioner for singularly perturbed problems, *SIAM J. Sci. Comput.*, 19(1998), 87-110.